

See discussions, stats, and author profiles for this publication at: <https://www.researchgate.net/publication/231641432>

# Carbon-Supported Manganese Oxide Nanoparticles as Electrocatalysts for the Oxygen Reduction Reaction (ORR) in Alkaline Medium: Physical Characterizations and ORR Mechanism

ARTICLE in THE JOURNAL OF PHYSICAL CHEMISTRY C · DECEMBER 2006

Impact Factor: 4.77 · DOI: 10.1021/jp0647986

---

CITATIONS

200

---

READS

84

4 AUTHORS, INCLUDING:



I. Roche

PSA PEUGEOT CITRÖEN

17 PUBLICATIONS 587 CITATIONS

SEE PROFILE



Marian Chatenet

Ecole de Physique, Electronique et Matériaux...

151 PUBLICATIONS 2,527 CITATIONS

SEE PROFILE

# Carbon-Supported Manganese Oxide Nanoparticles as Electrocatalysts for the Oxygen Reduction Reaction (ORR) in Alkaline Medium: Physical Characterizations and ORR Mechanism

I. Roche,<sup>†</sup> E. Chaînet,<sup>†</sup> M. Chatenet,<sup>\*,†</sup> and J. Vondrák<sup>‡</sup>

Laboratoire d'Electrochimie et de Physico-chimie des Matériaux et des Interfaces (LEPMI-ENSEEG, UMR 5631 CNRS-INPG-UJF), BP 75, 38402 Saint Martin d'Hères Cedex, France, and Institute of Inorganic Chemistry, Academy of Sciences of the Czech Republic, 250 68 Řež near Prague, Czech Republic

Received: July 27, 2006; In Final Form: November 3, 2006

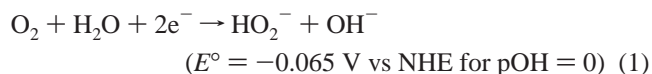
MnO<sub>x</sub>/C and Me-MnO<sub>x</sub>/C (Me = Ni, Mg) electrocatalysts prepared by chemical deposition of manganese oxide nanoparticles on carbon have been characterized by Transmission Electron Microscopy (TEM), X-ray Diffraction (XRD), and chemical analysis. Their Oxygen Reduction Reaction (ORR) kinetics and mechanism have been investigated in alkaline KOH solutions by using the Rotating Disk Electrode (RDE) and the Rotating Ring-Disk Electrode (RRDE) setups. Doping the MnO<sub>x</sub>/C nanoparticles with nickel or magnesium divalent cations can considerably improve their oxygen reduction activity. As a result, the Me-MnO<sub>x</sub>/C electrocatalysts exhibit ORR specific or mass activities close to the benchmark 10 wt % Pt/C from E-TEK. At low ORR current densities, the undoped MnO<sub>x</sub>/C electrocatalyst displays a reaction order with respect to P<sub>O<sub>2</sub></sub> and OH<sup>−</sup> of 1 and −0.5, respectively, while ∂E/∂log *i* is ca. −59 mV dec<sup>−1</sup>. The ORR reaction order toward OH<sup>−</sup> is unchanged with the magnesium doping, while it becomes −2 with the nickel doping. RRDE data show that doping the MnO<sub>x</sub>/C electrocatalysts directs the ORR toward the four-electron pathway. The first electrochemical step of the 4-electron ORR mechanism is probably the quasiequilibrium proton insertion process into MnO<sub>2</sub> leading to MnOOH, while the second electron transfer, consisting of the O<sub>2,ads</sub> species electrosplitting, yielding O<sub>ads</sub> and hydroxide anion, is rate determining. The presence of the doping metal cations may stabilize the intermediate Mn<sup>III</sup>/Mn<sup>IV</sup> species, which assist this second charge transfer to oxygen adatoms. As a result, the ORR rate is enhanced for the Me-MnO<sub>x</sub>/C electrocatalysts: they exhibit remarkable ORR catalytic activity and yield quantitative formation of OH<sup>−</sup> (selectivity toward the 4-electron pathway).

## 1. Introduction

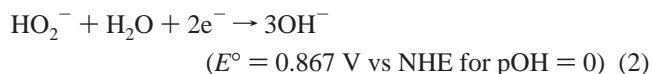
Platinum is known to be the best electrocatalyst for the Oxygen Reduction Reaction (ORR) in an alkaline fuel cell cathode.<sup>1</sup> However, for simple cost reasons, nonplatinized electrocatalysts have retained the focus of the scientific community for a long time. For example, the first H<sub>2</sub>/O<sub>2</sub> alkaline fuel cell, presented by Bacon<sup>2</sup> in 1933, used nickel oxide containing lithium on the cathode and nickel-based electrocatalysts on the anode. Since Bacon's work, many other metals or oxides have been studied in air electrodes: Pd, Ir, Co, Ru, Ni,<sup>3</sup> Ag/C,<sup>4–9</sup> or even macrocycles, usually based on nitrogen-containing ligands and transition metal cations.<sup>10</sup> Another promising material is manganese dioxide thanks to its great (electro)chemical stability, low cost, and rather high activity toward oxygen reduction.<sup>11–16</sup> Moreover, as primary battery materials,<sup>17</sup> manganese oxides have the ability to absorb or deliver a high quantity of charge in a short time: such a process, known as the flywheel effect, can advantageously be used in the air-cathode of fuel cells, as demonstrated by Vondrák et al.<sup>16</sup>

Brenet first summarized the electrochemical properties of manganese dioxide in alkaline aqueous solution.<sup>18</sup> Their elec-

trochemical activity toward the ORR in alkaline medium results from the presence of H atoms and OH groups at the manganese oxide surface. Several other authors, such as Kozawa and Yeager,<sup>19</sup> tried to determine the ORR mechanism on manganese oxides. However, uncertainties are still remaining, probably following their complex chemistry: MnO<sub>2</sub>, Mn<sub>2</sub>O<sub>3</sub>, and Mn<sub>3</sub>O<sub>4</sub> either hydrated or anhydrous may coexist, each of these species displaying a great variety of crystallographic structures and different electrochemical activities.<sup>20</sup> For Mao et al.,<sup>21</sup> the ORR mechanism of OH<sup>−</sup> production on MnO<sub>x</sub> can be described by a partial reduction with 2 electrons yielding hydrogen peroxide ions HO<sub>2</sub><sup>−</sup>:



either followed by the 2-electron reduction of HO<sub>2</sub><sup>−</sup>



or by the purely chemical disproportionation reaction of HO<sub>2</sub><sup>−</sup> in solution



Since manganese oxides exhibit excellent activity for HO<sub>2</sub><sup>−</sup> disproportionation reaction into O<sub>2</sub> and OH<sup>−</sup>,<sup>14,21</sup> the oxygen

\* Address correspondence to this author. Phone: +33 476 82 65 88. Fax: +33 476 82 67 77. E-mail: marian.chatenet@lepmi.inpg.fr.

<sup>†</sup> Laboratoire d'Electrochimie et de Physico-chimie des Matériaux et des Interfaces.

<sup>‡</sup> Institute of Inorganic Chemistry, Academy of Sciences of the Czech Republic.

replenished from (3) can be further reduced in (1). The overall process consists of an *apparent* 4-electron ORR mechanism, as also observed for carbon-supported platinum<sup>22</sup> or silver<sup>9</sup> nanoparticles.

The resulting overall four-electron O<sub>2</sub> reduction into OH<sup>−</sup> is as follows:



For manganese oxides as well as for more classical electrocatalysts (e.g., platinum and silver), it is now well admitted that the four-electron O<sub>2</sub> reduction into OH<sup>−</sup> (eq 4) can compete with the 2-electron pathway (eq 1) yielding HO<sub>2</sub><sup>−</sup> species.<sup>23–24</sup> These anions are corrosive and can generate problems of electrochemical cell premature degradation, like membrane alteration or electrode materials corrosion.<sup>9,25</sup> To prevent such failure of the fuel cell system, it is mandatory to be able to measure the amount of HO<sub>2</sub><sup>−</sup> anion formed as a function of the electrode potential, and better, to prevent their formation or decompose them. In that extent, manganese oxides are interesting, since one of the oldest known catalysts for hydrogen peroxide decomposition is precisely β-MnO<sub>2</sub>.<sup>26</sup> More recently, it has been shown that mixed and composite oxides in the spinel or perovskite structures were also active toward the hydrogen peroxide decomposition.<sup>27–28</sup> Among the numerous varieties of manganese oxides, manganite (MnOOH) exhibits the best catalytic activity toward the hydrogen peroxide disproportionation reaction.<sup>21</sup>

We point out at that stage that the manganese oxides studied in the literature so far were micro-sized more than nano-sized. We recently investigated the synthesis and characterization of the ORR activity in alkaline medium for nanostructured manganese oxide/carbon-based electrocatalysts.<sup>29</sup> Our preliminary conclusions were that the activity of such MnO<sub>x</sub>/C electrocatalyst nanoparticles, doped by various metal cations (nickel or magnesium), approaches that of a benchmark ORR electrocatalyst: 10 wt % Pt/C (E-TEK). In addition, we did roughly estimate the overall number of electrons (*n*<sub>o</sub>) exchanged per oxygen molecule, from the Koutecky–Levich slope determined from Rotating disk Electrode (RDE) measurements.<sup>29</sup> We found *n*<sub>o</sub> ≈ 2 at low cathodic overpotentials ( $|\eta_{\text{O}_2}| < 0.39 \text{ V}$ ), whereas *n*<sub>o</sub> ≈ 4 at high cathodic overpotentials, inducing negligible hydrogen peroxide yield at high ORR overpotentials. However, such Koutecky–Levich determination of *n*<sub>o</sub> is not very accurate. As a result, this previous paper could neither provide clear insight into the ORR mechanism for MnO<sub>x</sub>/C materials nor give an explanation about their good ORR kinetic parameters, especially due to lack of physical characterizations (only XRD analysis had been performed thoroughly). Thus, the present article aims at (i) fulfilling the MnO<sub>x</sub>/C physical characterization (with a special emphasis on high-resolution transmission electron microscopy (HR-TEM) coupled with energy dispersive X-ray analysis (EDS)), (ii) proposing an ORR mechanism for our carbon-supported manganese oxide nanoparticles in alkaline medium, with regard to the influence of the experimental conditions, and (iii) trying to link their high ORR activity with their physicochemical properties. Three samples have been considered: MnO<sub>x</sub>/C, either raw (undoped) or doped with nickel or magnesium divalent cations. The high area (around 1000 m<sup>2</sup> g<sup>−1</sup>) carbon substrate was also investigated without manganese oxide nanoparticles for comparison.

Our MnO<sub>x</sub>/C-based nanomaterials have first been thoroughly characterized in terms of physicochemical properties: the MnO<sub>x</sub>

nanoparticle size distribution, dispersion over the carbon substrate, chemical composition, and the possible existence of phase segregation were all investigated from HR-TEM and EDS coupling, whereas the overall metal loading was determined from elemental analysis.

Second, we studied their kinetic parameters toward the ORR, as a function of the oxygen partial pressure, solution pH (OH<sup>−</sup> activity), and temperature. From these data, we tried to estimate the most probable reaction mechanism and to compare it to classical ORR on electrocatalyst like carbon-supported platinum nanoparticles.

## 2. Experimental Section

**2.1. Synthesis of MnO<sub>x</sub>/C-Based Catalysts.** The C-supported MnO<sub>x</sub> preparation was described in a previous paper.<sup>13</sup> Quickly, 4 g of carbon black Chezacarb SH (Chemopetrol, Litvinov) was mixed with an aqueous solution of KMnO<sub>4</sub> and MnSO<sub>4</sub> (Lachema n.p., Brno, Czech Republic), corresponding to 2.4 g of Mn. The suspension was maintained at a controlled temperature (80 °C) for 15 min and then filtered and dried at 110 °C. Chezacarb SH is a hydrophilic carbon black (pH close to 8)<sup>13</sup> designed as sorbent to remove nonpolar substances from aqueous solutions; its specific area is ca. 1000 m<sup>2</sup> g<sup>−1</sup>.

A solution of Ni(NO<sub>3</sub>)<sub>2</sub>·6H<sub>2</sub>O or Mg(NO<sub>3</sub>)<sub>2</sub>·6H<sub>2</sub>O (Lachema n.p., Brno, Czech Republic) was added prior to the permanganate addition to prepare the Ni or Mg-doped catalysts, as described by Bezdička et al.<sup>13</sup>

**2.2. Physicochemical Characterizations of the Carbon-Supported MnO<sub>x</sub>/C-Based Materials.** According to their elaboration procedure (see section 2.1), the raw or doped MnO<sub>x</sub> nanoparticles are supported onto carbon black. We investigated their particle size distribution using high-resolution transmission electron microscopy (HR-TEM, Jeol 2010). For statistical relevance of the analysis, at least 1000 particles were counted for each sample (4 representative photographs, taken in random locations of the considered sample). The composition of the doped manganese oxide nanoparticles has also been evaluated from energy dispersive X-ray spectroscopy (EDS) coupled to the TEM: the spectra were obtained by lowering the electron beam down to nanometric size, so as to monitor only the fluorescence of the desired area of the sample (see section 3.1.1).

In addition, X-ray Diffraction (XRD) experiments have been undertaken for the three MnO<sub>x</sub>/C-based materials, on a Philips TW 1730 vertical goniometer/diffractometer equipped with a diffracted-beam monochromator, using Fe Kα radiation and recalculated for the Cu Kα radiation.

All the MnO<sub>x</sub>/C-based catalysts did exhibit a [Mn/(C + Mn + O)] loading around 20 wt % at the time of their synthesis.<sup>13,16</sup> From chemical analysis in the service central d'analyse (CNRS, Vernaison, France) we verified the actual loadings of each component for the three MnO<sub>x</sub>/C electrocatalysts (see section 3.1.2). Using the manganese loading values, we calculated the current densities with respect to the mass of active materials and evaluated the carbon impurities. Coupling these loading data with the TEM and XRD results also enables us to evaluate the approximate active area of the electrocatalysts and to further determine the specific activity (current densities divided by the specific area of the electrocatalyst) for our various samples.

**2.3. Materials and Electrodes.** A glassy carbon tip ( $\phi = 5 \text{ mm}$ ) was used as a substrate to characterize the active layers of the desired catalysts.<sup>9,25</sup> Each active layer was deposited from an ink containing 25 mg of MnO<sub>x</sub>/C, Ni-MnO<sub>x</sub>/C, or Mg-MnO<sub>x</sub>/C powder, 1 mL of water, 0.6 mL of ethanol, and 3 μL of PTFE beads in solution (60 wt %, DuPont).<sup>29</sup> After

homogenization by sonication, a 10  $\mu\text{L}$  drop of the ink was deposited on the glassy carbon electrode; the solvents were then evaporated at room temperature for 30 min. The resulting 2  $\mu\text{m}$  thick<sup>9</sup> porous active layer (containing 14 wt % PTFE on the basis of the dry materials) was then heat treated at 180  $^{\circ}\text{C}$  for 15 min to ensure its mechanical stability.

We used a Rotating Ring-Disc Electrode (RRDE DT21 + AFASR rotator, Pine) to evaluate the ORR mechanism on the  $\text{MnO}_x/\text{C}$ -based catalysts. The disk consisted of a glassy carbon rod ( $\phi = 5$  mm) and the ring was platinum.<sup>30</sup> Each active layer, around 4  $\mu\text{m}$  thick, was deposited on the disk from a 20  $\mu\text{L}$  drop of the inks described previously, no thermal treatment being applied to sinter the layer.

All solutions were prepared with (18.2  $\text{M}\Omega\text{ cm}$ , 3 ppb) water (Millipore, Elix + Milli-Q gradient) and Prolabo (Normapur) potassium hydroxide.

**2.4. Electrochemical Setups.** RRDE measurements were performed in 0.1 M KOH solution in a four-electrode cell. A platinum foil was used as the counter electrode and the RRDE disk and ring as working electrodes, while the reference was  $\text{Hg}-\text{HgO}$  in 1 M KOH (+0.1 V vs NHE): all potentials are nevertheless referred to the normal hydrogen electrode (NHE). The voltammetry experiments were conducted with a computer-controlled multichannel potentiostat (VMP2, Biologic Science Instruments) in the bistat configuration. The ORR voltammeteries were carried out after oxygen saturation of the electrolyte (20 min bubbling), the oxygen concentration being kept constant at its saturation value by gentle  $\text{O}_2$  (4.5-Messer) bubbling in the solution. The solution temperature was thermostated at  $25 \pm 1$   $^{\circ}\text{C}$ . Successive ORR voltammograms were recorded on the  $\text{MnO}_x/\text{C}$ -based active layers (immobilized as the porous active layer on the glassy-carbon disk) from 0.3 to  $-0.5$  V vs NHE in quasi-steady-state conditions ( $1 \text{ mV s}^{-1}$ ) in  $\text{O}_2$ -saturated potassium hydroxide solutions for various RRDE revolution speeds. Prior to each voltammetry, the potential was kept for 2 min at the starting potential, 0.3 V vs NHE, to ensure an identical initial surface state in all experiments. During the whole voltammetry at the disk, the ring potential was maintained at 0.45 V vs NHE: such potential is sufficiently high to enable the complete oxidation of any  $\text{HO}_2^-$  ions reaching the ring by centrifugal flow due to the rotation of the RRDE, while sufficiently low to hinder any  $\text{O}_2$ -evolution reaction. As a result, only the  $\text{HO}_2^-$  oxidation reaction is possible on the platinum ring. The ring ( $I_R$ ) and disk ( $I_D$ ) currents were measured simultaneously and plotted as a function of the disk ORR potential  $E_D$ . The collection efficiency  $N = I_R/|I_{D2e^-}|$ , corresponding to the percentage of  $\text{HO}_2^-$  ions formed on the disk which are detected on the ring, was checked by using experimental values of  $I_R$  and  $I_D$  (see section 3.4). For the classical<sup>31</sup> redox couple  $\text{Fe}(\text{CN})_6^{3-}/\text{Fe}(\text{CN})_6^{4-}$ , we found 0.336 at 500 rpm. The  $N$  mathematical expression only depends on the DT21 RRDE geometric characteristic dimensions:<sup>32</sup>  $N = 0.394$ , which means that 39.4% of a product formed on the disk should reach the ring. Such a calculated value agrees with the manufacturer data.<sup>30</sup> The small differences between the experimental and theoretical (calculated) values are probably due to the actual shape of our porous active layers (which are around 4  $\mu\text{m}$  thick), inducing turbulences that can slightly disturb the  $\text{HO}_2^-$  collection on the ring. Because such turbulences increase with increasing RRDE revolution speeds, our experiments were not performed above 2500 rpm. The number of electrons ( $n_t$ ) exchanged per reduced  $\text{O}_2$  molecule was calculated in the ORR potential range from the measured disk currents  $I_D$ , the ring

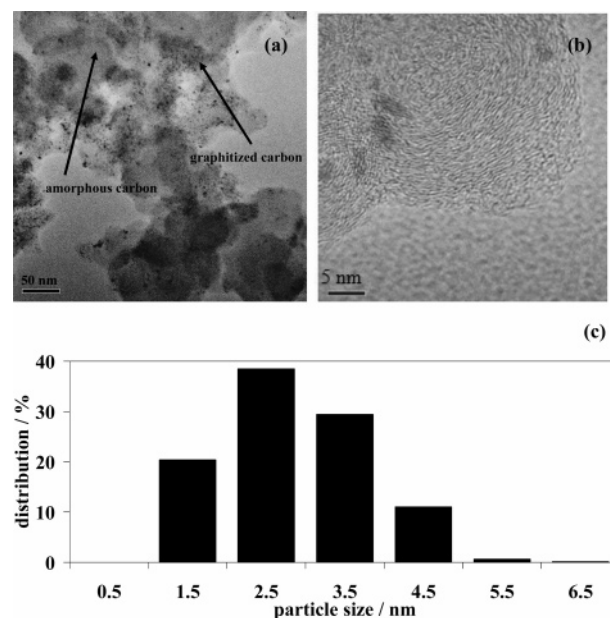


**Figure 1.** TEM (a) and HREM (b) images and corresponding particle-size distribution for  $\text{MnO}_x/\text{C}$ -1005 counted particles (c).

currents for peroxide oxidation  $I_R$ , and the collection efficiency  $N$ , according to eq 5:<sup>33</sup>

$$n_t = 4|I_D|/(|I_D| + I_R/N) \quad (5)$$

The electronic  $x^e$  and molar  $x^m$  proportions of  $\text{HO}_2^-$  ions formed on the disk were determined by starting from  $n_t$  values in the ORR potential range, according to the procedures described in refs 24, 33, and 34.

Similar RDE electrochemical measurements were performed in a molar KOH solution in a four electrode Pyrex cell connected to a computer-controlled potentiostat (PAR EG&G, model 273).<sup>29</sup> The ORR experiments were carried out after oxygen ( $P_{\text{O}_2} = 1.0$  atm) or air ( $P_{\text{O}_2} = 0.2$  atm—Messer:  $\text{N}_2$  78.09 vol %,  $\text{O}_2$  20.94 vol %,  $\text{H}_2$  500 ppm,  $\text{CO}_2$  330 ppm) saturation of the electrolyte. Blank experiments under argon atmosphere (4.5-Messer) were also performed to characterize the active layers in terms of active area (Pt/C) or stability in the ORR potential range ( $\text{MnO}_x/\text{C}$ -based materials).

### 3. Results

#### 3.1. Physicochemical Characterizations of the Carbon-Supported $\text{MnO}_x/\text{C}$ -Based Materials.

**3.1.1. TEM Characterization.** Figure 1a and Figure 1b show representative TEM and HR-TEM images for the  $\text{MnO}_x/\text{C}$  electrocatalysts. They exhibit good dispersion of the  $\text{MnO}_x$  particles over carbon. However, two distinct regions can be observed: some where carbon is graphitized, as revealed by the graphite diffraction fringes in Figure 1b, and others where it is amorphous. Most of the  $\text{MnO}_x$  particles are deposited on the graphitized zones of carbon, in agreement with the ability of metal nanoparticles to form  $\pi$ -complexes with multiple  $-\text{C}-\text{C}-$  bonds at the edge of graphene networks. In our case, the stability of the  $\pi$ -complexes may be increased by the oxygen-containing groups of manganese oxide nanoparticles in close proximity of the graphene  $>\text{C}=\text{C}<$  bonds.<sup>35</sup> The  $\text{MnO}_x$  particle dispersion over carbon is relatively homogeneous on graphitized areas, but worse on amorphous carbon. According to the TEM images, some agglomerates or particles having a diameter above 10 nm exist but in a very limited number: little aggregation



**TABLE 1: Mean XRD or TEM Particle Diameters for MnO<sub>x</sub>/C or Pt/C Electrocatalysts, Mass Activities (MA) and Specific Activities (SA) Measured at 0 V vs NHE, and Tafel Slopes for the ORR in O<sub>2</sub>-Saturated Molar KOH Solution at 25 °C**

| catalysts              | <i>d</i> /nm | MA/A g <sup>-1</sup> | SA/μA cm <sup>-2</sup> | <i>b</i> /V dec <sup>-1</sup> |
|------------------------|--------------|----------------------|------------------------|-------------------------------|
| MnO <sub>x</sub> /C    | 3.4–4.2      | 11.3                 | 3.2–4.0                | −0.057                        |
| Ni-MnO <sub>x</sub> /C | 4.3–6.0      | 39.6                 | 14.3–19.9              | −0.056                        |
| Mg-MnO <sub>x</sub> /C | 4.3–6.1      | 23.7                 | 8.5–12.2               | −0.047                        |
| 10 wt % Pt/Vulcan XC72 | 1.8          | 40.1                 | 25.8                   | −0.081                        |

phenomena seem to have occurred during the MnO<sub>x</sub>/C nanoparticles elaboration procedure.

The particle sizes distribution was estimated considering the Féret diameter, average of the maximum and minimum Féret diameters: Figure 1c shows the particle size distribution histogram for the MnO<sub>x</sub>/C electrocatalyst, determined neglecting the few agglomerated or very large nanoparticles. A total of 1005 particles were counted on the various representative TEM images relative to this sample, yielding satisfying statistics. The MnO<sub>x</sub>/C nanoparticles particle volume/area averaged diameter was calculated to be  $d_{v/a} = 3.4$  nm (see Table 1) according to the formula

$$d_{v/a} = \frac{\sum f_i d_i^3}{\sum f_i d_i^2} \quad (6)$$

where  $f_i$  is the ratio of particles having the diameter  $d_i$ .

The particle diameter distribution supports the little agglomeration statement made above: no particle sizes higher than 8 nm (ca. 3 times the average) were measured.

The MnO<sub>x</sub>/C electrocatalyst was also characterized by XRD (Table 1). The volume average diameter of the MnO<sub>x</sub> nanocrystalline domains,  $d_v = 4.2$  nm, was calculated from the XRD peaks with use of the Scherrer equation.<sup>36</sup> The TEM and XRD diameters for the MnO<sub>x</sub>/C electrocatalyst are very close, revealing the TEM observations were indeed representative of the overall material structure and that no detrimental amounts of large nanocrystallites were formed upon synthesis. However, nanoparticle agglomerates are not evidenced by XRD patterns, and we point out that we could hardly find any by TEM, which probably rules out the MnO<sub>x</sub> nanoparticle quantitative agglomeration upon synthesis.

The analysis of the Ni-MnO<sub>x</sub>/C or Mg-MnO<sub>x</sub>/C electrocatalysts (see the examples of Figure 2a and Figure 2c for the Ni-doped electrocatalyst) gave the particle distribution of Figure 2b and Figure 2d. As for the MnO<sub>x</sub>/C electrocatalyst, amorphous and graphitized carbon areas are observed: the Ni-MnO<sub>x</sub> particles seem to be in a great majority on the graphitized areas. Moreover, two different particle families are observed: one where there is approximately twice as much manganese than nickel and another where the ratio is reversed, as revealed by the EDS spectra monitored in the appropriate region of the electrocatalyst (not shown). The family where nickel prevails is characterized by the existence of particles homogeneous in diameter (Figure 2b), whereas that where manganese predominates is characterized by smaller nanoparticles, both well dispersed in size and over the carbon substrate (Figure 2d). We calculated two Ni-MnO<sub>x</sub> particle size distribution histograms relative to the Féret diameter for each different particle composition. Average diameters of  $d_{v/a} = 5.4$  (nickel-rich nanoparticles) and  $d_{v/a} = 2.2$  nm (manganese-rich nanoparticles) were calculated with a rather narrow distribution size. The XRD patterns do not reveal the existence of segregated nickel domains, showing that the nickel divalent cation was inserted in the MnO<sub>x</sub> crystal lattice (real doping). The average MnO<sub>x</sub>

particle diameter calculated from XRD spectra (disregarding the particle composition) from the Scherrer equation is 6.0 nm (Table 1). The TEM particle sizes for the two families are consistent with the XRD results, showing the TEM photograph were indeed representative of the whole sample.

The TEM images for the Mg-MnO<sub>x</sub>/C electrocatalyst (not shown for brevity) also support the existence of two distinct families of Mg-MnO<sub>x</sub> nanoparticles, although it is not as clear as in the case of Ni-doped catalysts. The overall average diameter can nevertheless be calculated:  $d_v = 4.3$  and 6.1 nm from TEM and XRD, respectively (Table 1).

**3.1.2. Materials Loadings.** The results from the chemical analysis are presented in Table 2 for each sample as well as that for the raw carbon black substrate: Chezacarb SH. The potassium and hydrogen loadings increase for all the MnO<sub>x</sub>/C-based materials compared to raw carbon, following the synthesis process of the carbon-supported manganese oxide nanoparticles. The carbon impurities are mainly N, S, Na, and Si, their mass loadings being less than 0.3 wt %. Table 2 gives doping metal loadings respectively of ca. 5.30 and 2.21 wt % for Ni-MnO<sub>x</sub>/C and Mg-MnO<sub>x</sub>/C materials. The manganese loadings are equal to 13.82, 10.82, and 19.88 wt % respectively for MnO<sub>x</sub>/C, Ni-MnO<sub>x</sub>/C, and Mg-MnO<sub>x</sub>/C. These last values will be taken into account for the calculation of the mass activities (MA) assuming MnO<sub>2</sub> is the active material. Let us notice that manganese loadings are less important than those given in previous papers,<sup>13,16</sup> for the material characterization closely following their synthesis. This shows how important it is to characterize the very material used in the electrochemical study (same material, same batch, same aging, etc.). The oxygen weight loading could not be measured, but probably corresponds to ca. 50 wt % of each sample (determined by subtraction, assuming the sum of the weight percentages relative to the elements investigated in Table 2 reaches 100 wt %) reflecting (i) the high oxidation degree of the high area carbon substrate (surface oxygenated groups) and (ii) the probable existence of the hydrated MnO<sub>x</sub> phase.<sup>37</sup>

**3.2. Influence of O<sub>2</sub> Pressure and OH<sup>-</sup> Concentration on the ORR Pathway.** For a multistep reaction like ORR, the rate determining step (rds) approximation, given in a general way by eq 7, provides insight into the mechanism where  $\alpha'$  is a

$$i \propto K C_{O_2}^\alpha C_{OH^-}^\beta \exp[-\alpha' n F E / (RT)] \quad (7)$$

symmetry factor and  $\alpha$  and  $\beta$  are respectively the fractional reaction orders with respect of the oxygen concentration ( $C_{O_2}$ ) and the OH<sup>-</sup> concentration ( $C_{OH^-}$ ) in the electrolyte under the applied oxygen pressure. As a result, the experimental conditions (e.g., temperature, pH, oxygen partial pressure:  $P_{O_2}$ ) should influence the measured ORR steady-state current density. Measuring the experimental values  $(\partial E / \partial \log P_{O_2})_{i, pH}$ ,  $(\partial E / \partial \log i)_{i, P_{O_2}}$ , and  $(\partial E / \partial pH)_{i, P_{O_2}}$  (simply noted  $\partial E / \partial \log P_{O_2}$ ,  $\partial E / \partial \log i$ , and  $\partial E / \partial pH$ , respectively) yields the coefficients  $\alpha$ ,  $\alpha'$ , and  $\beta$ . From these, the rds of the ORR mechanism can be isolated.

We attempted to determine the fractional reaction order  $\alpha$  (with respect to  $C_{O_2}$ ) value for our MnO<sub>x</sub>/C electrocatalysts. To do so,  $\partial E / \partial \log P_{O_2}$  was calculated from RDE results at 25 °C in a molar KOH solution for two different oxygen partial pressures: air and pure oxygen (see the example of Figure 3a for  $i(E)$  curves obtained on the Ni-MnO<sub>x</sub>/C active layer). The kinetic current densities  $i_k$  were calculated after correction from the O<sub>2</sub> diffusion in solution<sup>38</sup> and represented in the Tafel plane (Figure 3b). Such correction is usually insufficient at high cathodic overpotentials<sup>24–25</sup> (see the Appendix); thus we only

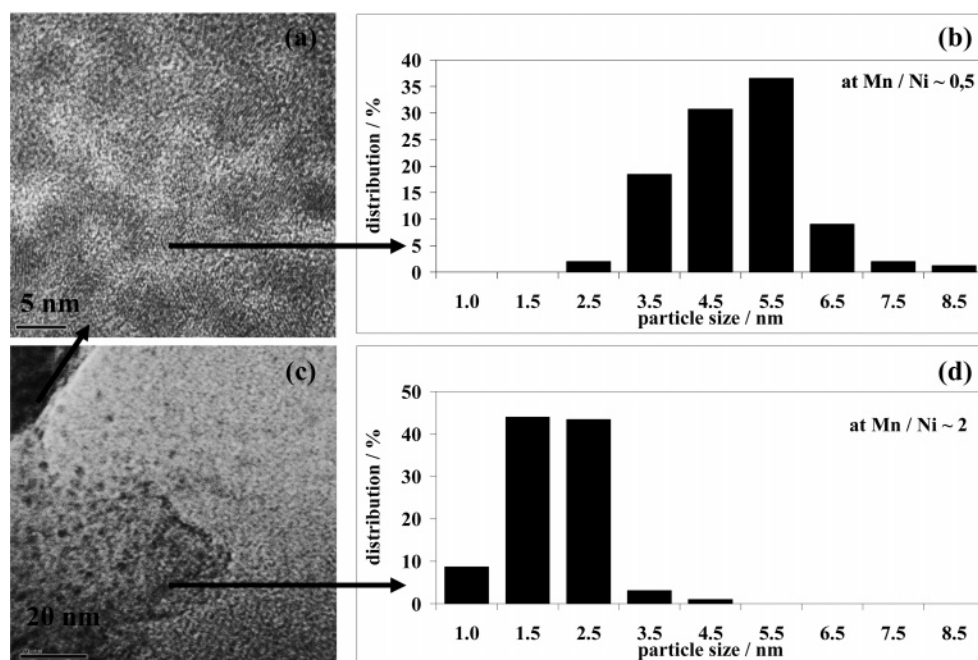


**Figure 2.** TEM images for Ni-MnO<sub>x</sub>/C, Mn/Ni  $\sim 0.5$  (a) and Mn/Ni  $\sim 2$  (c) and corresponding particle sizes distributions: Mn/Ni  $\sim 0.5$ , 244 counted particles (b), and Mn/Ni  $\sim 2$ , 842 counted particles (d).

**TABLE 2: Chemical Analysis for the MnO<sub>x</sub>/C Electrocatalysts**

|                        | C/wt % | Mn/wt % | Me/wt % | K/wt %   | H/wt % |
|------------------------|--------|---------|---------|----------|--------|
| MnO <sub>x</sub> /C    | 22.36  | 13.82   | -       | 3.28     | 2.84   |
| Ni-MnO <sub>x</sub> /C | 19.99  | 10.82   | 5.30    | 0.41     | 2.20   |
| Mg-MnO <sub>x</sub> /C | 38.04  | 19.88   | 2.21    | 1.83     | 1.51   |
| carbon black           | 92.43  |         |         | <500 ppm | 0.68   |

considered the low ORR current densities range ( $E > 0$  V vs NHE), where the limitation by the O<sub>2</sub> diffusion in the active layer is negligible. In addition, the pure faradic current under O<sub>2</sub> or air is obtained after subtraction from the blank current under argon in the same voltammetry sweep condition, for which nonnegligible hydrogen insertion occurs in the manganese oxide lattice. Starting from these Tafel voltammograms, we calculated the  $i_{k,1atm}/i_{k,0.2atm}$  ratio in the low overpotentials range:  $i_{k,1atm}/i_{k,0.2atm} = 4.1$ , 4.3, and 3.4 for MnO<sub>x</sub>/C, Ni-MnO<sub>x</sub>/C, and Mg-MnO<sub>x</sub>/C, respectively. The corresponding fractional reaction orders with respect to C<sub>O2</sub> are respectively ca. 0.9, 0.9, and 0.7. Knowing that the oxygen concentration C<sub>O2</sub> slightly fluctuates with the air bubbling rate, we consider that  $\alpha$  is close to 1 for our electrocatalysts, in agreement with the usual values for platinum<sup>22,24</sup> or silver.<sup>9</sup> From these values, we determine  $\partial E/\partial \log P_{O_2}$ , averaged in the low current densities range: +0.052, +0.044, and +0.034 V dec<sup>-1</sup> for MnO<sub>x</sub>/C, Ni-MnO<sub>x</sub>/C, and Mg-MnO<sub>x</sub>/C, respectively (Table 3).

The fractional reaction order with respect to C<sub>OH</sub> ( $\beta$ ) was similarly found by plotting  $\partial E/\partial pH$  from RDE results at 25 °C in O<sub>2</sub>-saturated 1 (pH 13.8)<sup>39</sup> or 0.1 M (pH 12.9)<sup>39</sup> KOH solution. As previously, only low current densities were considered after correction of the potential deviation with pH (Hg-HgO in 1 M KOH reference potential deviation with pH ca. -0.053 V dec<sup>-1</sup> at 25 °C).<sup>40</sup> The Tafel plots  $E$  (log $|i_k|$ ) show the current densities increase with decreasing OH<sup>-</sup> concentrations.  $E$  vs pH and the resulting  $\partial E/\partial pH$  (log $|i_k|$ ) curves were then plotted in the low current densities range:  $\partial E/\partial pH = -0.040$ ,  $-0.120$ , and  $-0.031$  V dec<sup>-1</sup> for MnO<sub>x</sub>/C, Ni-MnO<sub>x</sub>/C, and Mg-MnO<sub>x</sub>/C, respectively (Table 3). These  $|\partial E/\partial pH|$  values strongly vary with the doping while that for MnO<sub>x</sub>/C decreases with decreasing current densities.

Finally, the Tafel slopes  $b = \partial E/\partial \log|i_k|$  were estimated in the low current density range (Table 1):  $b = -0.057$ ,  $-0.056$ , and  $-0.047$  V dec<sup>-1</sup> for MnO<sub>x</sub>/C, Ni-MnO<sub>x</sub>/C, and Mg-MnO<sub>x</sub>/C, respectively, at 25 °C. Let us notice that we did not measure the Tafel slopes at higher current densities (Figure 3) following the Koutecky–Levich corrections insufficiency (see the Appendix). Moreover, as the adsorption isotherm of oxygen species may differ at the surface of manganese oxide and platinum,<sup>4</sup> we might not have to consider two distinct Tafel slopes with respect to ORR overpotential.

**3.3. Electrochemical Stability and ORR Activity for the MnO<sub>x</sub>/C Electrocatalysts.** Whereas MnO<sub>x</sub>/C undergoes the reduction of metastable oxides in the ORR potential range, corresponding to the reversible proton insertion process<sup>29,41</sup>



the voltammograms reveal a very good cycling stability of nickel or magnesium-doped MnO<sub>x</sub>/C. We point out such reduction of birnessite or  $\delta$ -MnO<sub>2</sub> is irreversible.<sup>42</sup>

The MnO<sub>x</sub> doping with divalent metals is also beneficial regarding the ORR kinetics. Nickel- and magnesium-doped MnO<sub>x</sub>/C exhibit ORR activity close to that of Pt/C, when the current densities are corrected from the O<sub>2</sub> diffusion in solution. In O<sub>2</sub>-saturated 1 M KOH solution at 25 °C, MA = 40 and 24 A g<sup>-1</sup> at 0 V vs NHE for Ni- and Mg-doped MnO<sub>x</sub>/C versus 11 A g<sup>-1</sup> for undoped MnO<sub>x</sub>/C (Table 1). By comparison our benchmark 10 wt % Pt/C powder (E-TEK) exhibits a slightly higher mass activity: MA = 40 A g<sup>-1</sup> at 0 V vs NHE. Notice that we chose to calculate MA values with respect to the platinum mass or that of manganese dioxide. In the case of the MnO<sub>x</sub>/C electrocatalysts, we assumed the active material is MnO<sub>2</sub>, which is probably not strictly correct (manganite MnOOH could also be considered as the active material and we chose not to take into account the (little) mass of the doping divalent cation), but nevertheless enables comparison between our three electrocatalysts. Starting from MA values and considering both the XRD or TEM mean diameters, we calculated the range of specific activities (SA) for each

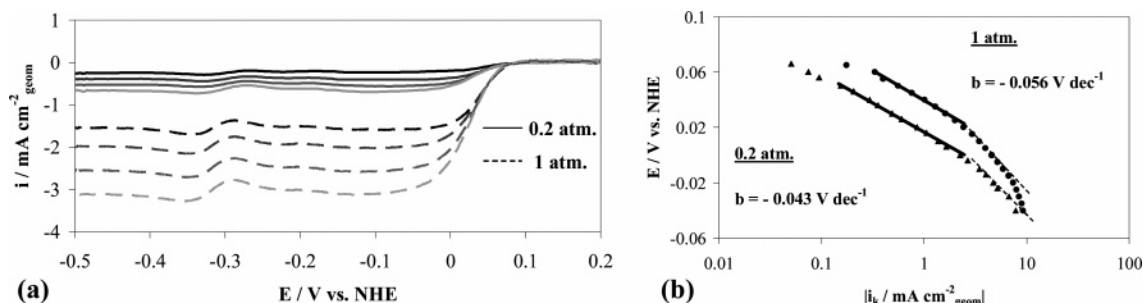


**Figure 3.** ORR voltammograms for Ni-MnO<sub>x</sub>/C for O<sub>2</sub> or air-saturated molar KOH solution, 25 °C;  $\nu_b = 0.001 \text{ V s}^{-1}$ , 500 (black), 900 (dark gray), 1600 (gray), or 2500 (light gray) rpm—currents corrected from the blank under argon (a). Corresponding Tafel representations (b).

**TABLE 3:**  $(\partial E/\partial \log|i|)_{i,\text{pH}}$ ,  $(\partial E/\partial \text{pH})_{i,P_{\text{O}_2}}$ , and  $(\partial E/\partial \log P_{\text{O}_2})_{i,\text{pH}}$ . Values in the Low Current Densities Range, for the MnO<sub>x</sub>/C Electrocatalysts

| catalysts              | $\text{V/dec}^{-1}$                                            |                                                      |                                                           |
|------------------------|----------------------------------------------------------------|------------------------------------------------------|-----------------------------------------------------------|
|                        | $(\partial E/\partial \log i_k )_{i,\text{pH},P_{\text{O}_2}}$ | $(\partial E/\partial \text{pH})_{i,P_{\text{O}_2}}$ | $(\partial E/\partial \log P_{\text{O}_2})_{i,\text{pH}}$ |
| MnO <sub>x</sub> /C    | -0.057                                                         | $-(0.040 \pm 0.005)$                                 | $+(0.052 \pm 0.007)$                                      |
| Ni-MnO <sub>x</sub> /C | -0.056                                                         | $-(0.120 \pm 0.015)$                                 | $+(0.044 \pm 0.004)$                                      |
| Mg-MnO <sub>x</sub> /C | -0.047                                                         | $-(0.031 \pm 0.002)$                                 | $+(0.034 \pm 0.003)$                                      |

electrocatalyst (Table 1). SA values for Me-MnO<sub>x</sub>/C electrocatalysts are higher than those for MnO<sub>x</sub>/C, especially in the case of the nickel doping: SA ranges from 14 to 20  $\mu\text{A cm}^{-2}$  MnO<sub>2</sub> and 9 to 12  $\mu\text{A cm}^{-2}$  at 0 V vs NHE for Ni-MnO<sub>x</sub>/C and Mg-MnO<sub>x</sub>/C, respectively, compared to 26  $\mu\text{A cm}^{-2}$  Pt for Pt/C.

**3.4. Proportion of Formed HO<sub>2</sub><sup>-</sup> Ions in the ORR Potential Range.** RRDE experiments were performed to determine quantitatively the ORR pathway, i.e., the relative formation rates of OH<sup>-</sup> and HO<sub>2</sub><sup>-</sup>, as a function of the electrode potential. As for the RDE experiments the pure faradic current under O<sub>2</sub> was obtained after subtraction from the *blank* current measured under argon in the same voltammetry sweep condition. Figure 4 shows  $I$  vs  $E_D$  curves obtained on the disk and the ring, for an active layer elaborated with Ni-MnO<sub>x</sub>/C. The voltammogram shape is similar for both doped and undoped MnO<sub>x</sub>/C electrocatalysts. As expected, the ring current is zero under argon atmosphere in the considered potential range (bold trace in Figure 4a). The benchmark results for Pt/C (2500 rpm) reveal the slightly lower peroxide formation for platinum than for all MnO<sub>x</sub>/C materials on the whole ORR potential range (Figure 4a), despite identical limiting plateaus for Pt/C and Ni-MnO<sub>x</sub>/C at the relevant RDE revolution rate (Figure 4b). We point out that the Pt/C slightly better ORR activity than for Ni-MnO<sub>x</sub>/C in 0.1 M KOH solution (as revealed by the higher ORR onset for Pt/C than for Ni-MnO<sub>x</sub>/C) may simply follow the detrimental pH dependence for ORR on Ni-MnO<sub>x</sub>/C ( $-120 \text{ mV dec}^{-1}$  vs  $-30$  or  $-60 \text{ mV dec}^{-1}$  for the Damjanovic<sup>43,46</sup> or Tarasevic<sup>10</sup> ORR mechanism on platinum, respectively). In molar KOH solutions, Pt/C and Ni-MnO<sub>x</sub>/C did not display different ORR activities (see Table 1).

$n_t$  was plotted as a function of the disk electrode potential  $E_D$  in the ORR potential range for each studied material at 500 rpm RRDE revolution speed. Figure 5 shows the resulting  $x^m(E_D)$  curves for the MnO<sub>x</sub>/C, Ni-MnO<sub>x</sub>/C, and Mg-MnO<sub>x</sub>/C electrocatalysts as well as that for the raw Chezacarb carbon. For MnO<sub>x</sub>/C,  $n_t = 3.54$  at +0 V vs NHE (low ORR overpotential), showing the ORR mechanism is mainly (but not totally, see Figure 4) oriented toward the 4-electron pathway. As a result, the peroxide anion yield is small: at  $E_D = +0 \text{ V}$  vs NHE, the electronic  $x^e$  and molar  $x^m$  percentages of HO<sub>2</sub><sup>-</sup> formed are respectively ca. 13% and 23% for MnO<sub>x</sub>/C compared to ca. 61% and 76% for the raw Chezacarb carbon (Table

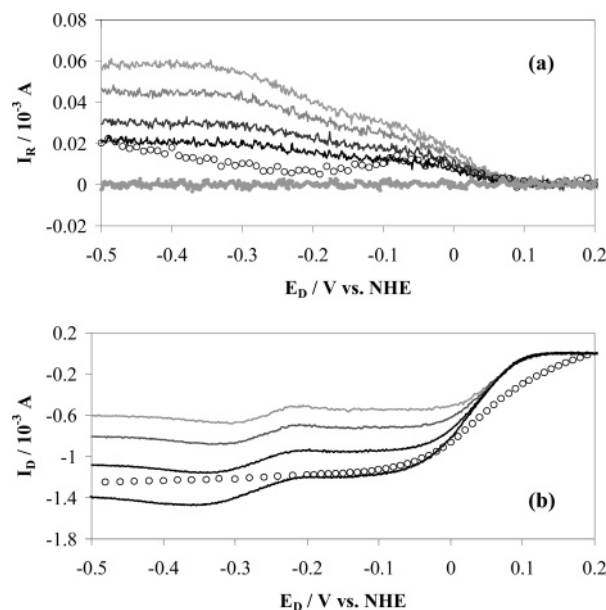


**Figure 4.** voltammograms of HO<sub>2</sub><sup>-</sup> oxidation at the ring (a) and ORR at the disk for Ni-MnO<sub>x</sub>/C (b); O<sub>2</sub>-saturated 0.1 M KOH solution at 25 °C,  $E_R = 0.45 \text{ V}$  vs NHE, 500 (black), 900 (dark gray), 1600 (gray), and 2500 (light gray) rpm,  $\nu_b = 0.001 \text{ V s}^{-1}$ —disk currents corrected from the blank under argon. Benchmark signal for Pt/C at 2500 rpm (open circles).

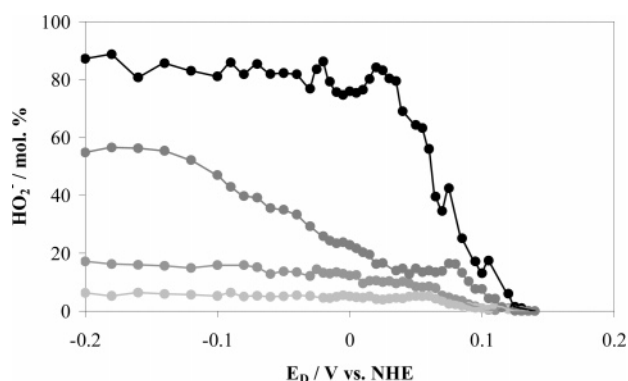


**Figure 5.** Molar production of HO<sub>2</sub><sup>-</sup> for carbon black Chezacarb (black), MnO<sub>x</sub>/C (dark gray), Mg-MnO<sub>x</sub>/C (gray), and Ni-MnO<sub>x</sub>/C (light gray), as a function of  $E_D$ ; O<sub>2</sub>-saturated 0.1 M KOH solution at 25 °C,  $E_R = +0.45 \text{ V}$  vs NHE, 500 rpm.

4). So, at this potential in O<sub>2</sub>-saturated 0.1 M KOH solution at 25 °C, approximately four times more oxygen moles are reduced to peroxide on raw carbon black than on MnO<sub>x</sub>/C. We point out that the peroxide yield is even higher for carbon at lower potentials:  $n_t \approx 2.35$  in the range  $[-0.4; 0] \text{ V}$  vs NHE, corresponding to  $x^e \approx 71\%$  and  $x^m \approx 83\%$ . This difference probably originates from the calculation uncertainty at low



**TABLE 4: Number of Electrons  $n_t$  Exchanged per Reduced  $O_2$  Molecule and Corresponding Electronic  $x^e$  or Molar  $x^m$  Proportions of  $HO_2^-$  Formed on a Disk at  $E_D = +0$  V vs NHE,  $O_2$ -Saturated 0.1 M KOH Solution at 25 °C,  $E_R = +0.45$  V vs NHE, 500 rpm**

| catalysts              | $n_t$             | $x^e/\%$        | $x^m/\%$        |
|------------------------|-------------------|-----------------|-----------------|
| MnO <sub>x</sub> /C    | 3.54              | 13              | 23              |
| Mg-MnO <sub>x</sub> /C | 3.75              | 6.6             | 12              |
| Ni-MnO <sub>x</sub> /C | 3.90              | 2.6             | 5.1             |
| Chezacarb carbon black | 2.48              | 61              | 76              |
|                        | 2.35 <sup>a</sup> | 71 <sup>a</sup> | 83 <sup>a</sup> |

<sup>a</sup> Values averaged in the relevant potential zone for ORR on carbon (0; -0.4 V vs NHE).

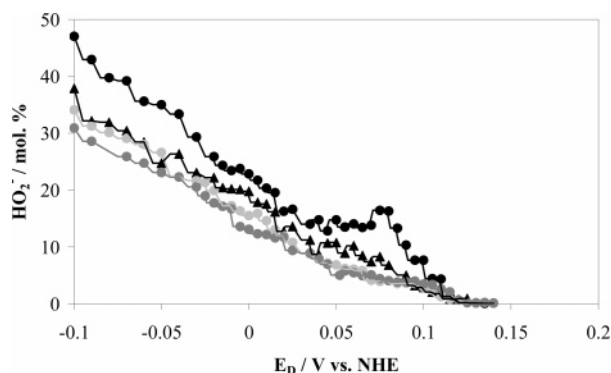


**Figure 6.** Molar production of  $HO_2^-$  for MnO<sub>x</sub>/C, as a function of  $E_D$ ;  $O_2$ -saturated 1 M (triangles) or 0.1 M (circles) KOH solution at 25 (black), 40 (gray), and 60 °C (light gray);  $E_R = +0.45$  V vs NHE, 500 rpm.

overpotentials, for which the ORR current at the disk for Chezacarb carbon active layers is small.

Doping the MnO<sub>x</sub>/C electrocatalysts by Ni or Mg further directs the oxygen reduction toward the 4-electron path and thus decreases the production of peroxide anion (Figure 5): at  $E_D = +0$  V vs NHE,  $n_t = 3.75$  and 3.90 for Mg-MnO<sub>x</sub>/C and Ni-MnO<sub>x</sub>/C, respectively. The corresponding molar proportions of  $HO_2^-$  formed are respectively 12% and 5.1% (Table 4). Thus, compared to MnO<sub>x</sub>/C, half the number of  $O_2$  molecules are reduced into  $HO_2^-$  in the case of Mg-MnO<sub>x</sub>/C and one-fifth for Ni-MnO<sub>x</sub>/C, revealing the doping benefit on the ORR pathway. This is of great interest regarding the long-term stability of the electrocatalysts and membrane during fuel cell operation.<sup>25</sup>

**3.5. Influence of Temperature and  $OH^-$  Concentration on the ORR Kinetics.** The ORR kinetics was studied for temperatures of 25, 40, and 60 ± 1 °C. As Figure 6 shows for the MnO<sub>x</sub>/C active layer, the ORR mechanism is directed toward the 4-electron pathway for increasing temperatures: the  $HO_2^-$  production decreases with increasing temperatures from 25 to 40 or 60 °C; the tendency is observed whether MnO<sub>x</sub>/C is doped or not. The apparent ORR activation energies ( $\Delta G_{act}^{app}$ ) for the MnO<sub>x</sub>/C electrocatalysts are evaluated at fixed overpotentials by using the Arrhenius equation.<sup>32</sup> After correction by the temperature variation of the Hg-HgO potential, we find  $\Delta G_{act}^{app} \approx 30$  kJ mol<sup>-1</sup> for all MnO<sub>x</sub>/C electrocatalysts in 0.1 M KOH at  $\eta_{O_2} = 0.26$  V, in agreement with literature data for platinum<sup>43,44</sup> or Pt/C<sup>4</sup> in alkaline medium.

Experiments similarly performed in  $O_2$ -saturated 0.1 and 1 M KOH solutions at 25 ± 1 °C showed the  $HO_2^-$  anion yield decreases with increasing  $OH^-$  concentrations (Figure 6), for either raw or doped MnO<sub>x</sub>/C electrocatalysts.

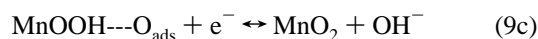
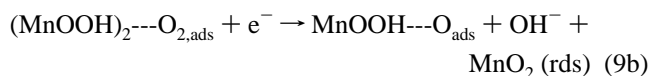
## 4. Discussion

**4.1. ORR Kinetics on the MnO<sub>x</sub>/C Electrocatalysts.** The electrochemical activity of manganese oxides depends on their crystalline structure. Cao et al.,<sup>45</sup> for example, showed that the ORR current observed at different MnO<sub>2</sub> catalysts increase in the following order:  $\beta$ -MnO<sub>2</sub> <  $\lambda$ -MnO<sub>2</sub> <  $\gamma$ -MnO<sub>2</sub> <  $\alpha$ -MnO<sub>2</sub>  $\approx$   $\delta$ -MnO<sub>2</sub>. They also found ORR mass activities close to those calculated in this work under air atmosphere in the low current densities range for  $\gamma$ -,  $\alpha$ -, and  $\delta$ -MnO<sub>2</sub>. Notice that our MnO<sub>x</sub> nanoparticles are supported onto the high specific area Chezacarb carbon, inducing the probable existence of different crystalline MnO<sub>2</sub> structure than in their work. As a result, our nanocrystalline MnO<sub>x</sub> exhibit higher activity toward the ORR than most microcrystalline MnO<sub>x</sub> electrocatalysts from the literature.

We think the dispersion of nanometric MnO<sub>x</sub> particles onto the high area carbon substrate improves their ORR activity especially in the low current density region. This benefit can result from a favorable particle size effect as already reported for platinum<sup>4,22,24</sup> or silver<sup>9</sup> nanoparticles (except in these latter cases the particle size effect is detrimental to the ORR activity), or a complete change in manganese oxide structural (and thus electrochemical) properties. The complete crystallographic characterization of our electrocatalysts is beyond the point of the present paper but will be developed in a forthcoming communication.

**4.2. The ORR Pathway on MnO<sub>x</sub>/C with Quantitative Hydroxide Yield.** The Tafel slope in the low current densities range is close to  $-2.3RT/F$  (i.e., -59 mV dec<sup>-1</sup> at 25 °C) in  $O_2$ -saturated KOH solution for MnO<sub>x</sub>/C. Taking into account the measurement uncertainties, the reaction order is the same (under air saturation) as that observed by Cao et al.<sup>45</sup> for  $\gamma$ -MnO<sub>2</sub> catalyst in air-saturated molar KOH solution at 25 °C.

The observed  $\partial E/\partial \log P_{O_2}$  dependence in the low current densities range ( $\approx +2.3RT/F$ ) is close to that observed for platinum by Damjanovic et al.<sup>46</sup> or Tarasevich et al.<sup>10</sup> The pH dependence also approaches that proposed for platinum by Damjanovic et al.<sup>46</sup> ( $+2.3RT/2F = -30$  mV dec<sup>-1</sup>) in the low current densities range at 25 °C. So, the ORR on MnO<sub>x</sub>/C obeys first-order kinetics toward the oxygen concentration but not toward the pH in alkaline solution. Our kinetic parameters are consistent with the following 4-electron ORR scheme on MnO<sub>x</sub>/C electrocatalyst in alkaline solution:



Reaction 8 is the proton insertion process. Reaction 9a corresponds to the  $O_2$  adsorption reaction, for which each oxygen molecule adsorbs onto two neighboring MnOOH sites at the electrode surface (bridged adsorption site). We think that Griffith or end-on adsorption is not likely to yield  $OH^-$ .<sup>10</sup> Reaction 9b is the second electron-transfer step and our rate determining step (rds), while reaction 9c is the reduction of  $O_{ads}$  species. This reaction pathway corresponds to an overall four-electron  $O_2$  reduction yielding  $OH^-$ . In such a scenario, the Mn<sup>III</sup>/Mn<sup>IV</sup> species act as oxygen acceptor/donor (mediator), as



noted by Vondrák et al.<sup>29</sup> or Ticianelli et al.<sup>47</sup> The coexistence of Mn<sup>III</sup> and Mn<sup>IV</sup> species is believed to assist the charge transfer to molecular (and adsorbed) oxygen and thus favor the oxygen reduction on MnO<sub>x</sub>/C. Hasan et al.<sup>48</sup> also showed that the presence of Mn species of different oxidation states in the same crystal lattice provides the necessary d–d electron mobility for high surface oxidoreduction activity. If we assume the chemisorption heat (for O<sub>ads</sub> and O<sub>2,ads</sub> species) decreases linearly with the surface coverage (Temkin isotherm), the rds equation in quasistationary conditions for such mechanism is then written

$$i_{(9b)} = nF\Gamma\theta_1 k_{\text{red}(9b)} \exp[-\beta_{\text{red}(9b)}fE] \exp[\alpha_1 r_1 \theta_1 + \alpha_2 r_2 \theta_2] \quad (10)$$

where  $\theta_1$  and  $\theta_2$  are respectively the surface coverage by O<sub>2,ads</sub> and O<sub>ads</sub> species,  $k_{\text{red}(9b)}$  is the kinetic constant of step 9b,  $r_1$  and  $r_2$  factors give the measurement of the O<sub>2,ads</sub> and O<sub>ads</sub> adsorption energy variation with the surface coverage,  $f = F/RT$ , and  $\Gamma$  is the overall number of sites, occupied or free, per unit of area of active material (MnO<sub>x</sub>).

The rate  $v_{(9a)}$  of the O<sub>2</sub> adsorption (9a) is given by

$$v_{(9a)} = K_{f(9a)} C_{O_2} \Gamma \theta_s - K_{b(9a)} \Gamma \theta_1 \quad (11)$$

where  $K_{f(9a)} = k_{f(9a)} \exp[-\alpha_{f(9a)}(r_1 \theta_1 + r_2 \theta_2)]$  and  $K_{b(9a)} = k_{b(9a)} \exp[\alpha_{b(9a)}(r_1 \theta_1 + r_2 \theta_2)]$ , with  $\alpha_{f(9a)} + \alpha_{b(9a)} = 1$ ;  $C_{O_2}$  is the O<sub>2</sub> concentration in the electrolyte, and  $\theta_s$  is the surface coverage of the MnO<sub>x</sub> free sites.

Step 9a is a quasiequilibrium, therefore  $v_{(9a)} = 0$  and

$$\theta_1 = (k_{f(9a)}/k_{b(9a)}) \theta_s C_{O_2} \exp[-(r_1 \theta_1 + r_2 \theta_2)] \quad (12)$$

If we assume that  $\theta_2$  is prevalent (which is consistent with a 4-electron pathway)<sup>46</sup>

$$i_{(9b)} = nFk_{\text{red}(9b)} (k_{f(9a)}/k_{b(9a)}) \exp[(\alpha_2 - 1)r_2 \theta_2] \exp[-\beta_{\text{red}(9b)}fE] \Gamma \theta_s C_{O_2} \quad (13)$$

The rate of the last step (reaction 9c) is given by

$$v_{(9c)} = K_{\text{red}(9c)} \Gamma \theta_2 - K_{\text{ox}(9c)} \Gamma \theta_s C_{OH^-} \quad (14)$$

where  $K_{\text{red}(9c)} = k_{\text{red}(9c)} \exp[\alpha_{\text{red}(9c)}r_2 \theta_2] \exp[-\alpha_{\text{red}(9c)}fE]$ ,  $K_{\text{ox}(9c)} = k_{\text{ox}(9c)} \exp[-\alpha_{\text{ox}(9c)}r_2 \theta_2] \exp[\alpha_{\text{ox}(9c)}fE]$ , with  $\alpha_{\text{red}(9c)} + \alpha_{\text{ox}(9c)} = 1$ ;  $C_{OH^-}$  is the OH<sup>−</sup> concentration in the bulk of the electrolyte.

As step 9c is a quasiequilibrium,  $v_{(9c)} = 0$ , and

$$\theta_s = 1 - \theta_2 = (\theta_2/C_{OH^-}) (k_{\text{red}(9c)}/k_{\text{ox}(9c)}) \exp[r_2 \theta_2] \exp[-fE] \quad (15)$$

Taking (15) into (13) yields

$$i_{(9b)} = nFk_{\text{red}(9b)} (k_{f(9a)}k_{\text{red}(9c)})/(k_{b(9a)}k_{\text{ox}(9c)}) \Gamma \theta_2 C_{O_2}/C_{OH^-} \exp[-(\beta_{\text{red}(9b)} + 1)fE] \exp[\alpha_2 r_2 \theta_2] \quad (16)$$

From the logarithm of (15),  $r_2 \theta_2$  becomes

$$r_2 \theta_2 = fE + \ln C_{OH^-} + \ln[(1 - \theta_2)/\theta_2] - \ln[k_{\text{ox}(9c)}/k_{\text{red}(9c)}] \quad (17)$$

Taking (17) into (16) and assuming  $\alpha_2 = \beta_{\text{red}(9b)} = 0.5$ , the rds equation for the low current densities region becomes

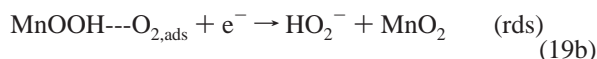
$$i_{(9b)} = X \exp[-fE] C_{O_2} C_{OH^-}^{-1/2} \quad (18)$$

with  $X = nF\Gamma k_{\text{red}(9b)} (k_{f(9a)}/k_{b(9a)}) (k_{\text{red}(9c)}/k_{\text{ox}(9c)})^{1/2} [\theta_2(1 - \theta_2)]^{1/2}$ .

The oxygen reduction at low current densities occurs at intermediate oxygen species coverage. The pH dependence of eq 18 is  $-2.3RT/2F$  following that of  $r_2 \theta_2$  given by (17), itself resulting from the quasiequilibrium of the last step (eq 9c), which follows the rds (Temkin isotherm). The expected pH dependence of (18) agrees with our results at 25 °C in O<sub>2</sub>-saturated molar KOH solution ( $-0.040$  V dec<sup>−1</sup> in the low current densities range) since  $|\partial E/\partial \text{pH}|$  decreases with decreasing current densities, which is consistent with our hypothesis: O<sub>ads</sub> surface coverage prevails in the low current densities range. In addition, let us point out that the adsorbed oxygen species coverage probably affects the reaction kinetics, especially concerning the pH dependence of (17). MnO<sub>x</sub>/C electrodes were not initially prerduced in this study, strengthening our *high adsorbed oxygen species coverage* hypothesis and the use of the Temkin isotherm.

Our experimental reaction order with respect to O<sub>2</sub> agrees with the proposed mechanism in the low current densities range ( $+0.052$  V dec<sup>−1</sup>). The oxygen partial pressure ( $\partial E/\partial \log P_{O_2} \approx +2.3RT/F$ ) and pH ( $\partial E/\partial \text{pH} \approx -2.3RT/2F$ ) dependences can originate from the state of quasiequilibrium for the steps preceding and following the rate determining step, the reaction intermediates being under the Temkin conditions of adsorption.

**4.3. The ORR Pathway on MnO<sub>x</sub>/C with Hydrogen Peroxide as an Intermediate.** Our RRDE experiments show that the 2-electron pathway yielding hydrogen peroxide ions is not negligible on MnO<sub>x</sub>/C in the low current densities range. The alternative 2-electron ORR scheme in alkaline medium can then be proposed:



Reaction 19a is the O<sub>2</sub> adsorption process. This adsorption step differs from that proposed in the case of the 4-electron O<sub>2</sub> reduction scheme, in a way that O<sub>2,ads</sub> species are only adsorbed onto a single MnOOH site (end-on or Griffith). Reaction 19b is the electron-transfer step. This pathway corresponds to a 2-electron O<sub>2</sub> reduction into HO<sub>2</sub><sup>−</sup> and results from the fact that the O=O bond cannot be broken with such end-on or Griffith adsorption of molecular oxygen.

This scheme can nevertheless be followed by either a 2-electron reduction of HO<sub>2</sub><sup>−</sup> ions or a disproportionation reaction of HO<sub>2</sub><sup>−</sup> in solution or on the MnO<sub>x</sub>/C nanoparticles, which display high activity toward this reaction.<sup>16,21</sup> As for the 4-electron pathway, we assume that the second electron-transfer step, reaction 19b, is the rds and that the chemisorption heat decreases linearly with the surface coverage

$$i_{(19b)} = nF\Gamma \theta k_{\text{red}(19b)} \exp[-\beta_{\text{red}(19b)}fE] \exp[\alpha r \theta] \quad (20)$$

where  $\theta$  is O<sub>2,ads</sub> surface coverage and  $k_{\text{red}(19b)}$  is the kinetic constant of step 19b. The factors  $r$  and  $\alpha$  have the same meaning as in section 4.2.

From the quasiequilibrium of step 19a, one obtains

$$\theta = k_{f(19a)}/k_{b(19a)} \theta_s C_{O_2} \exp[-r\theta] \quad (21)$$

We assumed that  $r\theta$  at intermediate coverage is given by

$$r\theta = fE \quad (22)$$

Taking (21) into (20), the rds becomes

$$i_{(19b)} = nFk_{\text{red}(19b)}k_{\text{f}(19a)}/k_{\text{b}(19a)}\Gamma(1 - \theta)C_{\text{O}_2}\exp[-fE] \quad (23)$$

with  $\alpha = \beta = 1/2$ .

In that case, the pH dependence is nil, following the pH independence of  $r\theta$  given by (22). Our experimental pH dependence of  $-0.040 \text{ V dec}^{-1}$  in the low current densities range does not support such a peroxide pathway. However, the ORR on graphite or on high specific area carbon black is well-known to quantitatively yield peroxide ions,<sup>1,24</sup> either in alkaline or in acid solutions.

From Figure 5, more than half the  $\text{O}_2$  molecules are indeed reduced to  $\text{HO}_2^-$  on the Chezacarb carbon in the overpotential range corresponding to the  $|i_k|$  value for which the pH dependence was determined (this proportion increases to ca. 80% in the ORR region where carbon reaches its maximum activity, i.e., below 0 V vs NHE). The corresponding number of electrons per oxygen molecule,  $n_t = 2.35$  to 2.48 (Table 4), is, however, higher than expected for carbon surfaces (which should yield quantitative peroxide generation and thus  $n_t = 2$ ).<sup>49</sup> High  $n_t$  values express that either some of the peroxide anions are decomposed or reduced in the active layer or that the carbon substrate also reduces oxygen in a parallel 4-electron pathway. We think the former scenario is more likely. Indeed, our active layers were rather thick ( $4 \mu\text{m}$  for RRDE experiments). In consequence,  $\text{HO}_2^-$  anions which have been formed in the volume of the carbon active layer should first diffuse within the active layer thickness before being able to reach its surface, be expelled by the electrode rotation, and finally undergo detection at the ring. The resulting average residence time for hydrogen peroxide anion is thus probably not negligible in our case. Knowing the Chezacarb carbon substrate displays high specific surface area (ca.  $1000 \text{ m}^2 \text{ g}^{-1}$ ), which results in high porosity into which  $\text{HO}_2^-$  anions might be trapped, goes in line with such a statement. High  $\text{HO}_2^-$  residence time is consistent with their spontaneous decomposition in solution (within the carbon active layer) or even more on the (high area) functionalized carbon (carbons with high surface area promote both peroxide generation and elimination reactions<sup>49</sup>).

Thus, part of the  $\text{HO}_2^-$  anions formed can originate from ORR on the carbon itself, and the experimental pH dependence of  $-0.040 \text{ V dec}^{-1}$  monitored for  $\text{MnO}_x/\text{C}$  does probably reflect the ORR  $\partial E/\partial \text{pH}$  contribution of the carbon substrate. We emphasize the fact that it is not possible to completely decorrelate the carbon and  $\text{MnO}_x$  ORR contributions, mainly following the extremely complex structure of our  $\text{MnO}_x/\text{C}$  electrocatalyst. Hydrogen peroxide decomposition is known to be favorable on manganese oxide catalysts<sup>50</sup> but its activation energy ( $E_a$ ) depends on the  $\text{MnO}_x$  particles crystalline structure and synthesis:<sup>48,51</sup>  $E_a = 77 \text{ kJ/mol}^{-1}$  in the  $20\text{--}35^\circ\text{C}$  range for manganese oxides obtained by calcination of  $\beta\text{-MnO}_2$ .<sup>48</sup> It also depends on the solution temperature, peroxide concentration, and pH. However, as (i) the ORR kinetic parameters are higher for the  $\text{MnO}_x$  electrocatalyst than for carbon and (ii) part of the  $\text{HO}_2^-$  anions formed inside the porous  $\text{MnO}_x/\text{C}$  active layer can be decomposed in the active layer (either spontaneously on the carbon or even more likely on the  $\text{MnO}_x/\text{C}$  nanoparticles),<sup>9,25</sup> the 4-electron pathway probably masks the 2-electron pathway. Finally, the experimental pH influence is consistent with a ORR mechanism on  $\text{MnO}_x$  strongly directed toward the 4-electron pathway, as shown by Calegari et al.<sup>52</sup> and suspected from our previous work.<sup>29</sup>

The experimental  $P_{\text{O}_2}$  dependence of  $+2.3RT/F$  is not affected by the competition between the 4-electron and the 2-electron pathways on  $\text{MnO}_x/\text{C}$ .

**4.4. Influence of the Nickel or Magnesium Doping on the ORR Pathway.** The RRDE experiments confirm our RDE results. The nickel or magnesium doping yields significantly decreased peroxide ions production in the low current densities range (Figure 5). The activation energy of the hydrogen peroxide decomposition also decreases with nickel doping.<sup>47</sup> Thus, the presence of the divalent (doping) cations would enable sufficiently fast peroxide elimination by the increase of  $\text{HO}_2^-$  decomposition kinetic, provided peroxide anions are indeed produced (for example on carbon). This elimination, however, seems to be less important in the case of the magnesium doping. The beneficial effect of nickel doping toward the oxygen reduction is explained<sup>13</sup> by the ability of transition metal atoms to exist in several states of valence, such as  $\text{Ni}(\text{OH})_2/\text{NiOOH}$ , and thus to assist the charge transfer to oxygen, leading to increased electronic interactions with the stabilized manganite species. We think the divalent cations indeed favor the stabilization of  $\text{Mn}^{\text{III}}/\text{Mn}^{\text{IV}}$  species.<sup>29</sup> The adsorption step (reaction 9a) has then an advantage compared to reaction 19a (more neighboring  $\text{MnOOH}$  sites are available) and the ORR mechanism is orientated toward the direct 4-electron pathway. As a result,  $\text{Ni-MnO}_x/\text{C}$  ORR electrochemical activity exceeds that of  $\text{Mg-MnO}_x/\text{C}$  (Table 1). The doping by nickel or magnesium also seems to modify the  $P_{\text{O}_2}$  influence. Moreover, the nickel doping changes the pH influence of the ORR mechanism that becomes  $-2.3(2RT/F)$ . It actually may change the pH dependence of the surface coverage by adsorbed oxygen species  $\text{O}_{\text{ads}}$ .

## 5. Conclusion

Materials prepared by chemical deposition of  $\text{MnO}_x$  on carbon were characterized with TEM, XRD, and chemical analysis. The  $\text{MnO}_x$  particles are nanometric in size and well dispersed on the carbon surface. We also successfully characterized these electrocatalysts for the ORR using the RDE and RRDE setups. Me-doped (Me = Ni, Mg)  $\text{MnO}_x/\text{C}$  exhibit remarkable ORR catalytic activity, close to the benchmark catalyst 10 wt % Pt/C from E-TEK, and yield quantitative formation of  $\text{OH}^-$  (4-electron pathway). Starting from our experiments, the first electrochemical step of the 4-electron ORR mechanism is suggested to be the quasiequilibrium proton insertion process in  $\text{MnO}_2$  leading to  $\text{MnOOH}$ ; the rate determining step is the second electron-transfer step consisting of the electrosplitting of the  $\text{O}_{2,\text{ads}}$  species, yielding  $\text{O}_{\text{ads}}$  and hydroxide anion.

**Acknowledgment.** This project was supported on the Czech side by the Grant Agency of Czech Republic (Project No. 104/02/0731), by the Grant Agency of Academy of Sciences (Nos. 403/002 and KJB 481 3302), and by the Ministry of Education of Czech Republic (Project No. MSM 262200010). It was also supported on the French side by the Ministry of Education and Research of France (Project No. PF 2002 88 2) and by the CNRS (Project No. 18105).

## Appendix: $\text{O}_2$ -diffusion limitations

The overall ORR current density on the RDE disk is given by eq 24:

$$1/|i| = 1/|i_1^{\text{diff}}| + 1/|i_k| \text{ where } 1/|i_1^{\text{diff}}| = 1/|i_1^{\text{diff, solution}}| + 1/|i_1^{\text{diff, active layer}}| \quad (24)$$

where  $i_k$  is the kinetic current density and  $i_1^{\text{diff. solution}}$  and  $i_1^{\text{diff. active layer}}$  are respectively the O<sub>2</sub> diffusion limiting current density in the electrolyte and in the active layer. For RDE experiments,  $i_1^{\text{diff. solution}}$  can be expressed from the classical Levich eq 25:<sup>32</sup>

$$|i_1^{\text{diff. solution}}| = 0.62n_l F C_{O_2} D_{O_2}^{3/2} \nu^{-1/6} \Omega^{1/2} = n_l B \Omega^{1/2} \quad (25)$$

In O<sub>2</sub>-saturated molar KOH solution, at 25 °C and atmospheric pressure,<sup>39</sup> the oxygen concentration, the oxygen diffusion coefficient, and the kinematic viscosity of the electrolyte are respectively  $C_{O_2} = 0.843 \times 10^{-6} \text{ mol cm}^{-3}$ ,  $D_{O_2} = 1.43 \times 10^{-5} \text{ cm}^2 \text{ s}^{-1}$ , and  $\nu = 0.01128 \text{ cm}^2 \text{ s}^{-1}$ . In O<sub>2</sub>-saturated 0.1 M KOH solution, at 25 °C,  $C_{O_2} = 1.210 \times 10^{-6} \text{ mol cm}^{-3}$ ,  $D_{O_2} = 1.87 \times 10^{-5} \text{ cm}^2 \text{ s}^{-1}$ , and  $\nu = 0.01013 \text{ cm}^2 \text{ s}^{-1}$ .<sup>39</sup>  $\Omega$  (rad s<sup>-1</sup>) represents the RDE revolution speed while  $B$  is the Levich slope.

In the case of a 20  $\mu\text{L}$  catalyst-containing ink deposit on the 0.196 cm<sup>2</sup> glassy carbon electrode,  $L$  is close to 4  $\mu\text{m}$ . For such thickness, the correction from O<sub>2</sub> diffusion in the active layer can be described by using the macrohomogeneous model,<sup>53</sup> for which the ohmic drop is neglected. Other models exist, such as the flooded agglomerates model.<sup>54</sup>  $i_1^{\text{diff. active layer}}$  can be expressed as the following relationship:<sup>32</sup>

$$i_1^{\text{diff. active layer}} = (n_l F C_{al} D_{al})/L \quad (26)$$

with  $D_{al}$  and  $C_{al}$  representing respectively the O<sub>2</sub> diffusion coefficient and the O<sub>2</sub> solubility in the active layer;  $L$  is the thickness of the active layer.

The results<sup>53</sup> show  $i_1^{\text{diff. active layer}}$  cannot be neglected for platinum at high ORR overpotentials, but the correction is unnecessary (even for platinum) at low ORR overpotentials.<sup>32</sup> Assuming platinum is a (slightly) better ORR electrocatalyst than MnO<sub>x</sub>/C (see Table 1), we only corrected the disk currents from the oxygen diffusion in solution, using the classical Koutecky–Levich model.<sup>38</sup> The validation of the un-necessity of such correction for MnO<sub>x</sub>/C catalysts at low ORR overpotentials as been shown recently for the ORR.<sup>55</sup>

## References and Notes

- (1) Kinoshita, K. In *Electrochemical Oxygen Technology*; J. Wiley and Sons: New York, 1992.
- (2) Bacon, F. T. *Beama J.* **1954**, *6*, 61.
- (3) Chang, C. C.; Wen, T. C. *Mater. Chem. Phys.* **1997**, *47*, 203.
- (4) Geniès, L. Thèse de doctorat, INPG, 1999.
- (5) Illiev, I.; Mrha, J.; Kaisheva, A.; Gamburgzev, S. *J. Power Sources* **1976**, *1*, 35.
- (6) Furuya, N.; Ichinose, O.; Uchimura, A. ISE meeting, Paris, 1997, abstract 611.
- (7) Zoval, J. V.; Stiger, R. M.; Biernacki, P. R.; Penner, R. M. *J. Phys. Chem.* **1996**, *100*, 837.
- (8) Zoval, J. V.; Biernacki, P. R.; Penner, R. M. *Anal. Chem.* **1996**, *68*, 1585.
- (9) Chatenet, M.; Geniès-Bultel, L.; Aurousseau, M.; Durand, R.; Andolfatto, F. *J. Appl. Electrochem.* **2002**, *32*, 1131.
- (10) Tarasevich, M. R.; Sadkowsky, A. E.; Yeager, B. In *Comprehensive Treatise of Electrochemistry*; Conway, B. E., O'M. Bockris, J., Yeager, E. B., White, R. E., Eds.; Plenum: New York, 1983; Vol. 7, p 301.
- (11) Zoltowski, P.; Drazic, D. M.; Vorkapic, L. *J. Appl. Electrochem.* **1973**, *3*, 271.
- (12) Vondrák, J.; Sedlaříková, M.; Novák, V. *J. New Mater. Electrochem. Syst.* **1998**, *1*, 25.
- (13) Bezdička, P.; Grygar, T.; Klápště, B.; Vondrák, J. *Electrochim. Acta* **1999**, *45*, 913.
- (14) Klápště, B.; Vondrák, J.; Velická, J. *Electrochim. Acta* **2002**, *47*, 2365.
- (15) Vondrák, J.; Klápště, B.; Velická, J.; Sedlaříková, M.; Černý, R. *J. Solid State Electrochem.* **2003**, *8*, 44.
- (16) Vondrák, J.; Klápště, B.; Velická, J.; Sedlaříková, M.; Novák, V.; Reiter, J. *J. New Mater. Electrochem. Syst.* **2005**, *8*, 1.
- (17) Scarr, R. F.; Hunter, J. C.; Slezacek, P. J. Alkaline Manganese dioxide batteries. In *Handbook of batteries*; Linden, D. L., Reddy, T. B., Eds.; McGraw-Hill: New York, 2002; Chapter 10.
- (18) Brenet, J. P. *J. Power Sources* **1979**, *4*, 183.
- (19) Kozawa, A.; Yeager, J. F. *J. Electrochem. Soc.* **1965**, *112*, 959.
- (20) Brock, S. L.; Duan, N.; Tian, Z. R.; Giraldo, O.; Zhou, H.; Suib, S. L. *Chem. Mater.* **1998**, *10*, 2619.
- (21) Mao, L.; Zhang, D.; Sotomura, T.; Nakatsu, K.; Koshiba, N.; Ohsaka, T. *Electrochim. Acta* **2003**, *48*, 1015.
- (22) Geniès, L.; Bultel, Y.; Faure, R.; Durand, R. *Electrochim. Acta* **2003**, *48*, 3879.
- (23) Chatenet, M. Thèse de doctorat, INPG, 2000.
- (24) Geniès, L.; Faure, R.; Durand, R. *Electrochim. Acta* **1998**, *44*, 1317.
- (25) Chatenet, M.; Aurousseau, M.; Durand, R.; Andolfatto, F. *J. Electrochem. Soc.* **2003**, *150*, D47.
- (26) Katz, K. *Adv. Catal.* **1953**, *5*, 173.
- (27) Goldstein, J. R.; Tseung, A. C. C. *J. Catal.* **1974**, *32*, 452.
- (28) Fahim, R. B.; Zaki, M. I.; El-Roudi, A. M.; Hassan, A. M. A. *J. Res. Inst. Catal. (Hokkaido Univ.)* **1981**, *29*, 25.
- (29) Vondrák, J.; Klápště, B.; Velická, J.; Sedlaříková, M.; Reiter, J.; Roche, I.; Chainet, E.; Fauvarque, J. F.; Chatenet, M. *J. New Mater. Electrochem. Syst.* **2005**, *8*, 209.
- (30) PINE Instrument Company, website <http://www.pineinst.com/echem/index.asp>, Rotated Ring-Disk Electrodes, DT21 Series Single-Piece RRDEs for AFASR Rotator, technical paper.
- (31) Damjanovic, A.; Genshaw, M. A.; O'M. Bockris, J. *J. Electrochem. Soc.* **1967**, *114*, 1107.
- (32) Bard, A. J.; Faulkner, L. R. *Electrochemical Methods*; Wiley & Sons: New York, 1980.
- (33) Alberly, W. J.; Hitchman, M. L. In *Ring-Disk Electrodes*; Oxford University Press: Oxford, UK, 1971; pp 17–28.
- (34) Antoine, O.; Durand, R. *J. Appl. Electrochem.* **2000**, *30*, 839.
- (35) Sachtler, W. M. H.; Stakheev, A. Y. *Catal. Today* **1992**, *12*, 283.
- (36) Warren, B. E. In *X-ray Diffraction*; Dover Publications Ed., Inc.: New York, 1990; p 251.
- (37) Anderson, T. N. *Modern Aspects of Electrochemistry*; White, R. E., Conway, B. E., O'M Bockris, J., Eds.; Plenum Press: New York, 1996; Vol. 30, Chapter 4.
- (38) Diard, J.-P.; Le Gorrec, B.; Montella, C. In *Cinétique électrochimique*; Herman: Paris, France, 1996.
- (39) Zinola, C. F.; Castro Luna, A. M.; Triaca, W. E.; Arvia, A. J. *J. Appl. Electrochem.* **1994**, *24*, 531.
- (40) *Handbook of Chemistry and Physics*; Weast, R. C., Ed.; Chemical Rubber Co.: Cleveland, OH, 1962; D-110.
- (41) Pourbaix, M. In *Atlas d'équilibres électrochimiques*; Gauthier-Villard: Paris, France, 1963.
- (42) McBreen, J. *Electrochim. Acta* **1975**, *20*, 221.
- (43) Sepa, D. B.; Vojnovic, M. V.; Damjanovic, A. *Electrochim. Acta* **1981**, *26*, 781.
- (44) Park, S.-M.; Ho, S.; Aruliah, S.; Weber, M. F.; Ward, C. A.; Venter, R. D. *J. Electrochem. Soc.* **1986**, *133*, 1641.
- (45) Cao, Y. L.; Yang, H. Y.; Ai, X. P.; Xia, L. F. *J. Electroanal. Chem.* **2003**, *557*, 127.
- (46) Damjanovic, A.; Brusica, V. *Electrochim. Acta* **1967**, *12*, 615.
- (47) Ticianelli, E. A.; Lima, F.; Calegario, M. 209th ECS spring meeting, Denver, 2006; Abstract 301.
- (48) Hasan, M. A.; Zaki, M. I.; Pasupulety, L.; Kumari, K. *Appl. Catal. A* **1999**, *181*, 171.
- (49) Kinoshita, K. In *Carbon, Electrochemical and Physicochemical Properties*; John Wiley and Sons: New York, 1988; No. 390, p 360.
- (50) Hess, W. T. Hydrogen Peroxide. In *Kirk-Othmer Encyclopedia of Chemical Technology*; Wiley and Sons: New York, 1995; Vol. 13.
- (51) Kanungo, S. B.; Parida, K. M.; Sant, B. R. *Electrochim. Acta* **1981**, *26*, 1157.
- (52) Calegario, M. L.; Lima, F. H. B.; Ticianelli, E. A. *J. Power Sources* **2006**, *158*, 735.
- (53) Gloaguen, F.; Andolfatto, F.; Durand, R.; Ozil, P. *J. Appl. Electrochem.* **1994**, *24*, 863.
- (54) Giner, J.; Hunter, C. *J. Electrochem. Soc.* **1969**, *116*, 1124.
- (55) Chatenet, M.; Micoud, F.; Roche, I.; Chainet, E.; Vondrák, J. *Electrochim. Acta* **2006**, *51*, 5452.